Supporting Information

Experimental Section

Synthesis of Materials:

Synthesis of ZIF-67 nanodices: In a typical synthesis, 4 mL of an aqueous solution containing 116 mg of $Co(NO_3)_2 \cdot 6H_2O$ and 2 mg of cetyltrimethylammonium bromide (CTAB) was rapidly injected into 28 mL of an aqueous solution containing 1.8 g of 2-methylimidazole and vigorously stirred at room temperature for 20 min. The precipitate was subsequently collected by repeatedly washing with ethanol for at least 5 times before vacuum drying it at room temperature overnight.

Synthesis of $CoSe_2$/C-ND: The as-prepared ZIF-67 nanodices and Se powder with mass ratio of 1:2 were uniformly mixed by grinding with a mortar and a pestle. This mixture was subsequently heated at 600 °C for 2 h with a ramping rate of 2 °C min^{-1} to obtain $CoSe_2$/C-ND.

Synthesis of $CoSe_2$/C-ND@rGO: $CoSe_2$/C-ND was first functionalized with a 0.5 wt% polydiallyldimethlammonium chloride (PDDA) aqueous solution containing 40 mM NaCl and 20 mM tris(hydroxymethyl)aminomethane. After stirring for 2 h, free PDDA was removed by centrifugation (three cycles), washing, and redispersion. Afterwards, a certain amount of GO suspension (mass ratio of $CoSe_2$/C-ND to GO: 1) was introduced, resulting in the self-assembly of the negatively-charged GO nanosheets and the positively-charged $CoSe_2$/C-ND via electrostatic attraction. After mild stirring at room temperature for 10 min, the $CoSe_2$/C-ND@GO film was collected by filtration under vacuum. Finally, the $CoSe_2$/C-ND@rGO film was obtained upon vacuum drying at 50 °C overnight and calcination at 500 °C in an argon atmosphere for 2 h with a ramping rate of 5 °C min^{-1}.

Ionic Liquid Electrolyte Preparation:

The ionic liquid electrolyte was prepared by slowly dissolving anhydrous aluminum chloride ($AlCl_3$) in 1-ethyl-3-methylimidazolium chloride ([EMIm]Cl) with a molar ratio of 1.3:1 upon stirring in an argon-atmosphere glove box ([O_2] < 0.01 ppm, [H_2O] < 0.01 ppm). The as-prepared ionic liquid electrolyte was settled for at least 12 h before its utilization.

Materials characterizations:

The samples were degassed under vacuum at 300 °C overnight before the adsorption measurements. Super-high purity N_2 (99.999%) was used for the physisorption measurements. The Brunauer–Emmett–Teller (BET) equation was used to calculate the apparent surface area from the adsorption data (P/P_0 between 0.05 and 0.2). The pore-size distributions of all samples were calculated by using the nonlocal density functional theory (NLDFT) method using the adsorption branch. The crystal structures of the samples were analyzed by powder X-ray diffraction (XRD, D8 Advance, Bruker, Germany) with CuKα radiation at 40 kV and 30 mA. The microscopic morphology and microstructure of the samples were observed by field-emission scanning electron microscopy (SEM, Sirion 200, FEI, Netherlands) and high-resolution transmission electron microscopy (HRTEM, Tecnai-G2-20-S-Twin, FEI, Netherlands). X-ray photoelectron spectroscopy (XPS, PHI 5000 Versa Probe, ULVAC-PHI, Japan) with an Al Kα X-ray source (1486.6 eV) was used to study the surface chemical composition and valent state of the elements of the samples. The Raman spectra were recorded using a 532-nm laser excitation at room temperature on a Raman spectrophotometer (DXR, Thermo Fisher Scientific). The zeta potentials of the samples were obtained using a zeta-potential analyzer (Zetasizer Nano ZS, Malvern Instruments, UK). The ^{27}Al NMR spectra of the samples were measured on a Bruker Advance 400 spectrometer using a 1.0 M $Al(NO_3)_3$ aqueous solution as an external chemical shift standard. The cobalt contents of the cell electrolytes were determined on an atomic absorption spectrometer (AAS, PG-990, PG-Instrument, England).

Fabrication of the Electrochemical Cell:

To prepare the cathodes, the as-prepared samples were ground together with acetylene black and polyvinylidene fluoride (PVDF) with a mass ratio of 6:3:1. After adding anhydrous ethanol as a dispersing agent, the mixture slurry was coated onto a rounded molybdenum current collector of 12 mm in diameter and dried at 80 °C under vacuum for 12 h. The amount of the active material loaded was ca. 1.5–2 mg. Aluminum foil (99.99%) served as an anode. The rechargeable aluminum-ion batteries (RAIBs) were assembled using a customized Swagelok-type cell in an argon-filled glove box at room temperature. Two layers of glass fiber paper (Whatman 934-AH) were placed between the Al anode and the cathode. 500 µL of the ionic liquid electrolyte was added to the cell to wet the separator adequately. The energy densities were calculated on the basis of the mass of active materials contained in both electrodes of the cell.

Electrochemical Measurements:

The galvanostatic charge/discharge measurements were performed over a potential range of 0.05–2.2 V versus Al/Al^{3+} on a LANHE battery tester. Cyclic voltammetry (CV) measurements were conducted at different scan rates over a range of 0.0–2.4 V versus Al/Al^{3+} on an electrochemical workstation (CHI 660E, Chenhua Instrument corporation, China) in a three electrode-mode (Reference electrode: Al strip; counter electrode: Al foil; and working electrode: samples on Mo foil).

Ex-situ Measurement Techniques:

For the ex-situ XRD studies, the electrodes were fully charged or discharged at a current density of 1000 mA g^{-1}. After fully charged to 2.2 V or discharged to 0.05 V, the Mo foil containing the cathode materials was removed from the cell in the glove box. To avoid reaction with atmospheric moisture or oxygen, the cathode with the Mo current collector downside was placed onto a glass slide and wrapped by a PI film. The wrapped samples were then immediately removed from the glove box for XRD measurements.

For ex-situ XPS and TEM studies, the fully charged or discharged cathodes were washed with propylene carbonate three times to remove the residual electrolyte. The cathodes were subsequently dried at 40 °C under vacuum for 12 h to remove the residual propylene carbonate. Finally, these samples were sealed in a plastic sample bottle to avoid contamination by moisture or oxygen before the measurements.

For the ex-situ NMR studies, the electrodes were fully charged or discharged at a current density of 1000 mA g^{-1}. After fully charged to 2.2 V or discharged to 0.05 V, the cathode materials were collected from the cell for NMR measurements in the glove box.

Computational Methods:

All the first-principles calculations were carried out in the periodic framework of density functional theory (DFT) with the program package DMol3, using the spin-polarized generalized gradient approximation (GGA) in the form of exchange-correlation functional PBE.
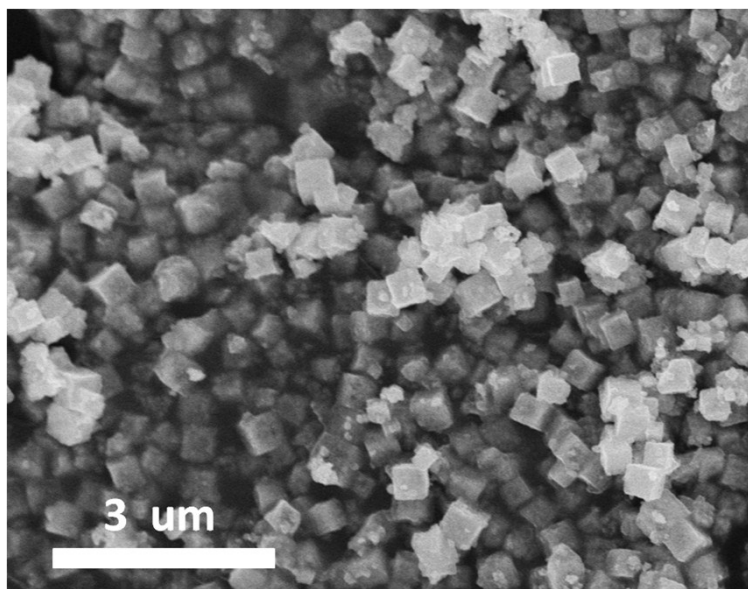
Fig. S1 SEM images of CoSe$_2$/C-ND
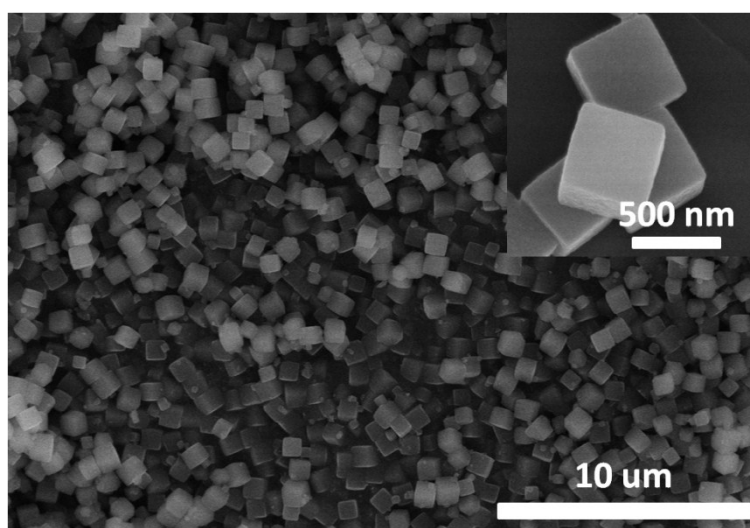
Fig. S2 SEM images of ZIF-67 nanodices

It is worth noting that the evolution of the hollow cavity and the porous shell of the CoSe$_2$/C-ND can be interpreted as a bulk version of the Kirkendall effect[1]. Specifically, the seleno-reactions between Se and Co mainly take place on the surface and the near surface region of the ZIF-67 because Se can not diffuse rapidly into the bulk phase of ZIF-67. On the other hand, Co can diffuse outward quickly to the near surface of ZIF-67 to react with Se. As a result, a hollow cavity was generated after the selenization process. Meanwhile, the removal of the organic groups of ZIF-67 at high temperature led to the formation of a carbon matrix and porous channels[2].
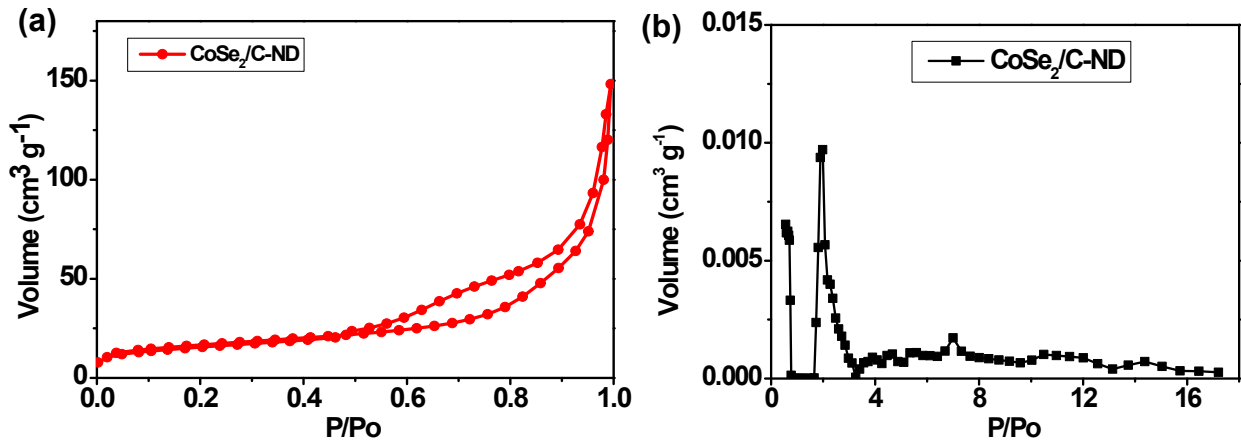
Fig. S3 (a) Nitrogen adsorption-desorption isotherms; (b) pore size distribution curves calculated by DFT method using adsorption branch

As shown in Fig. S3, the N_2 adsorption isotherms of $CoSe_2$/C-ND were type IV. The obvious hysteresis loop and the continuous accretion of nitrogen uptake at a relative pressure ranging from 0.4 to 1.0 demonstrate the existence of mesopores and macropores. The pore size distributions calculated by the density functional theory (DFT) method further revealed the hierarchical pore-structure of this sample. The specific surface area of $CoSe_2$/C-ND was 106 m^2 g^{-1}.
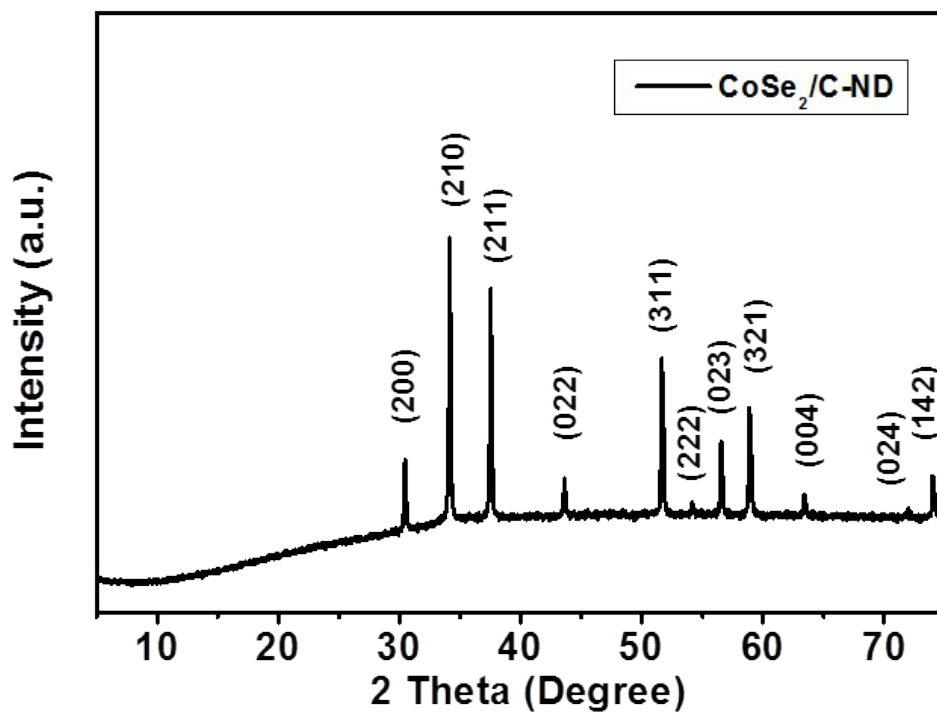
Fig. S4 The XRD pattern the CoSe$_2$/C-ND

The crystal structures of the as-synthesized samples were analyzed by powder XRD, as shown in Fig. S4. The XRD pattern showed the main peaks at 2θ = 30.5, 34.2, 37.6, 51.7, and 58.9°, which can be ascribed to the (200), (210), (211), (311), and (321) planes of a cubic CoSe$_2$ phase (PDF 00-010-0409)[3-5], respectively. No impurity was found, indicating that a high-purity cubic CoSe$_2$ was successfully prepared.
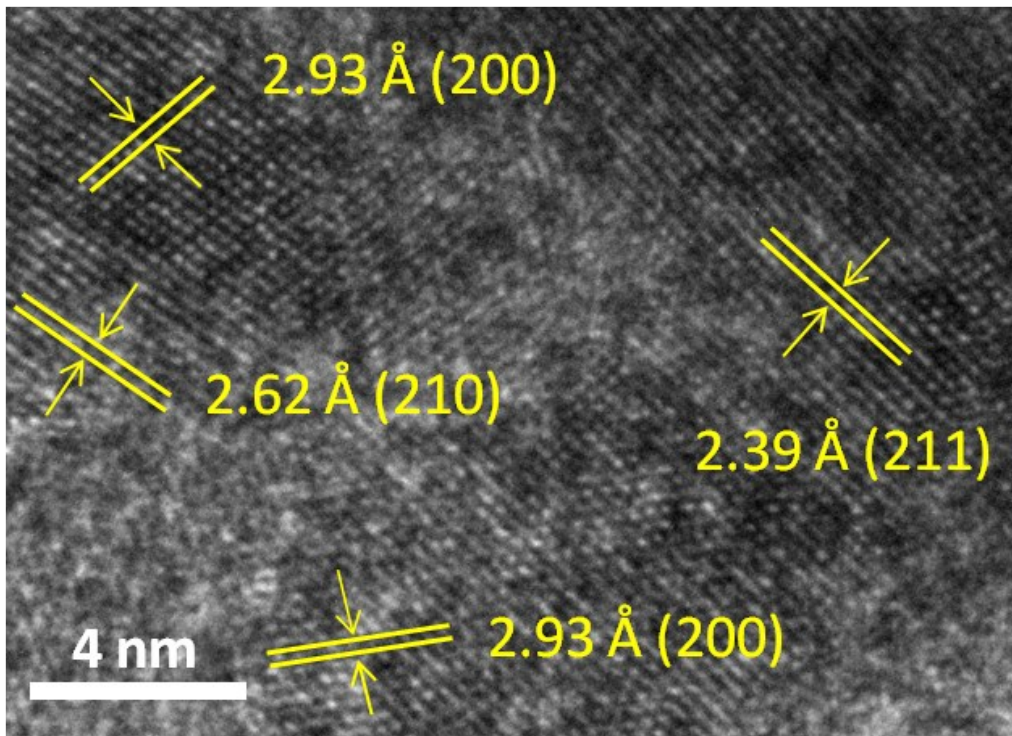
Fig. S5. HRTEM image of CoSe$_2$/C-ND.
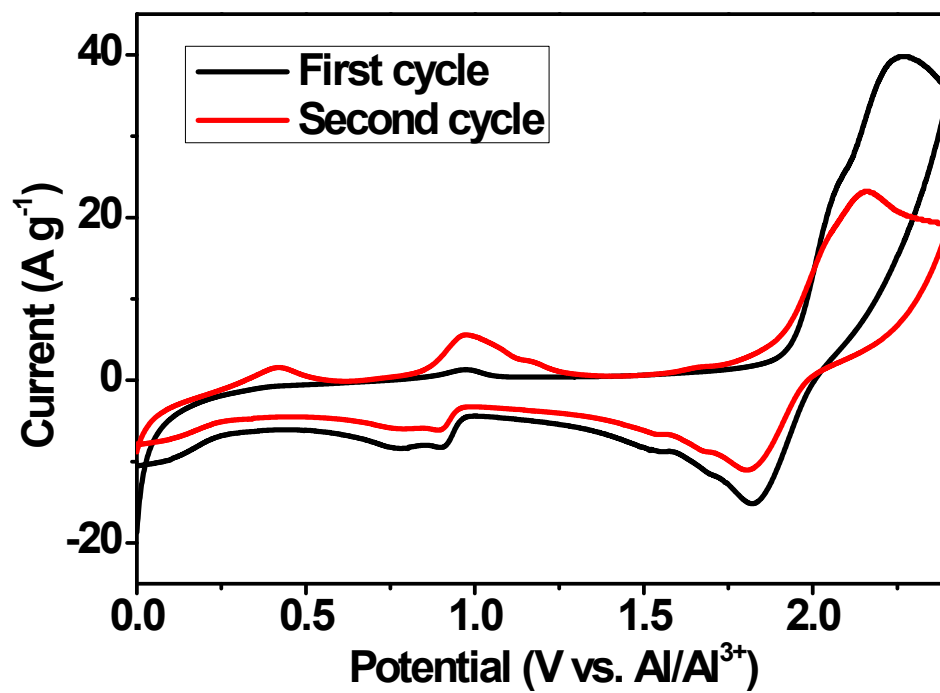
Fig. S6 Initial CV curves of CoSe$_2$/C-ND between 0 and 2.4 V.
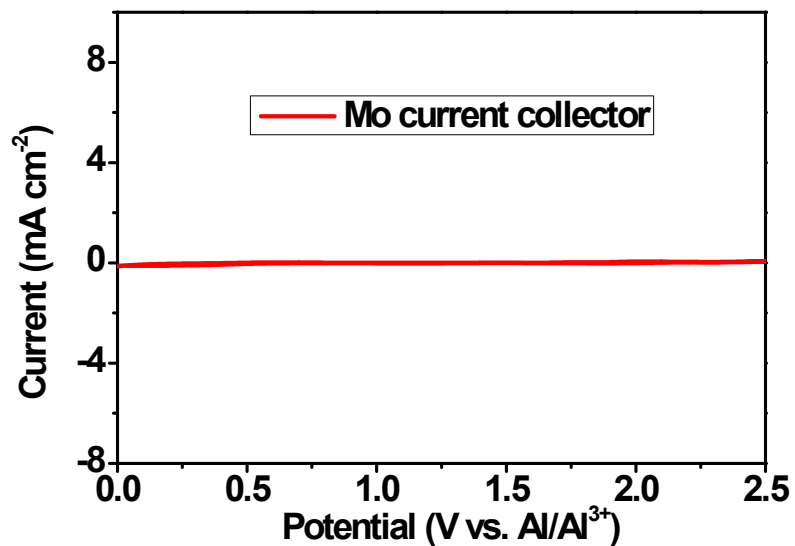
Fig. S7 Cyclic voltammetry curves of Mo foil at a scan rate of 10 mV s^{-1} against an Al reference electrode.

Before investigating the electrochemical performance of the as-prepared samples, we first evaluated the error that may be introduced by the Mo foil current collector. No redox peaks were observed in the CV curve of Mo foil, indicating the suitability of Mo foil as a current collector.
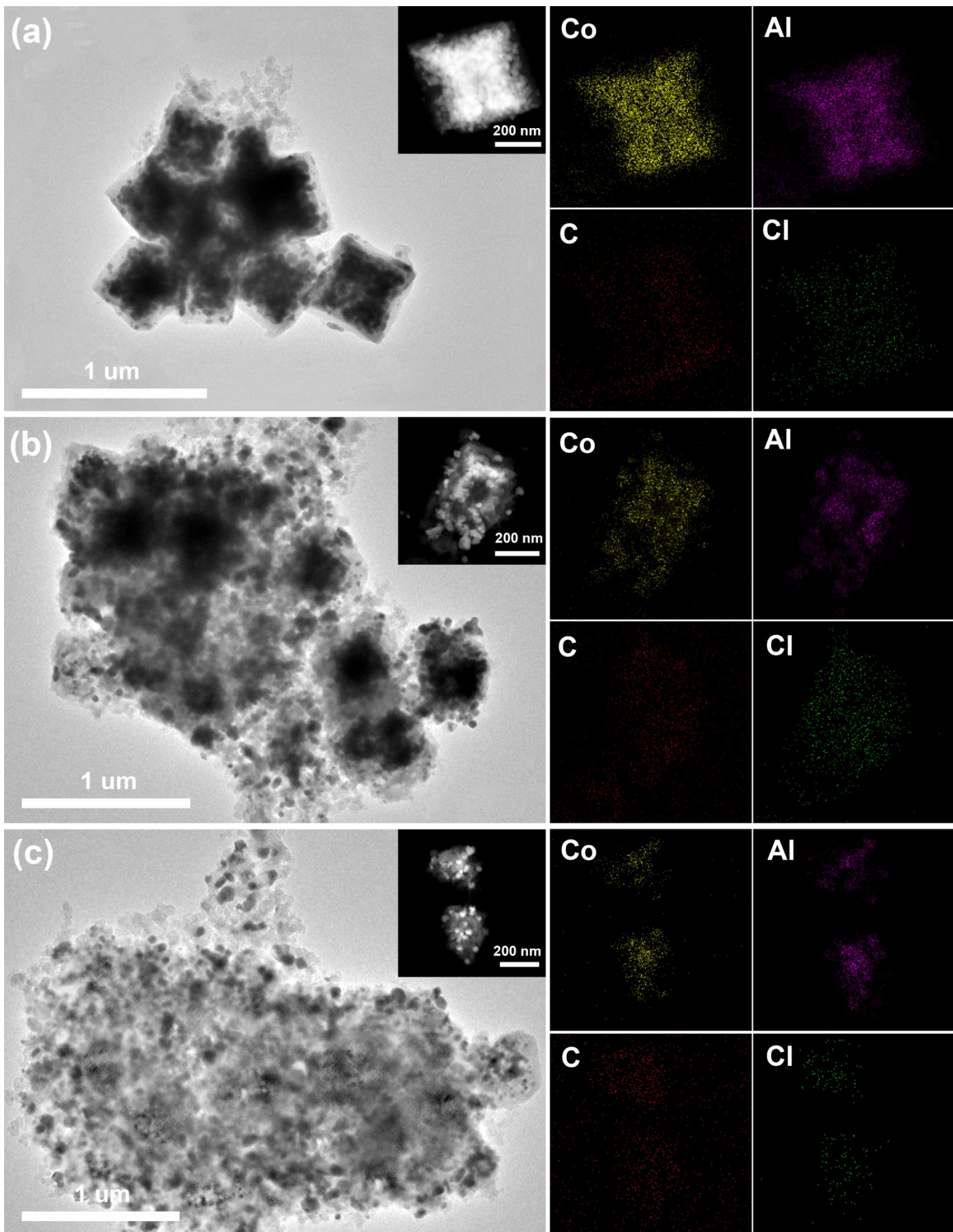
Fig. S8 TEM images and EDX (energy dispersive x-ray spectrometry) mapping images for Co, Al, Cl and C of the fully discharged CoSe$_2$/C-ND electrodes after 1 cycle (a), 100 cycles (b) and 500 cycles (c).
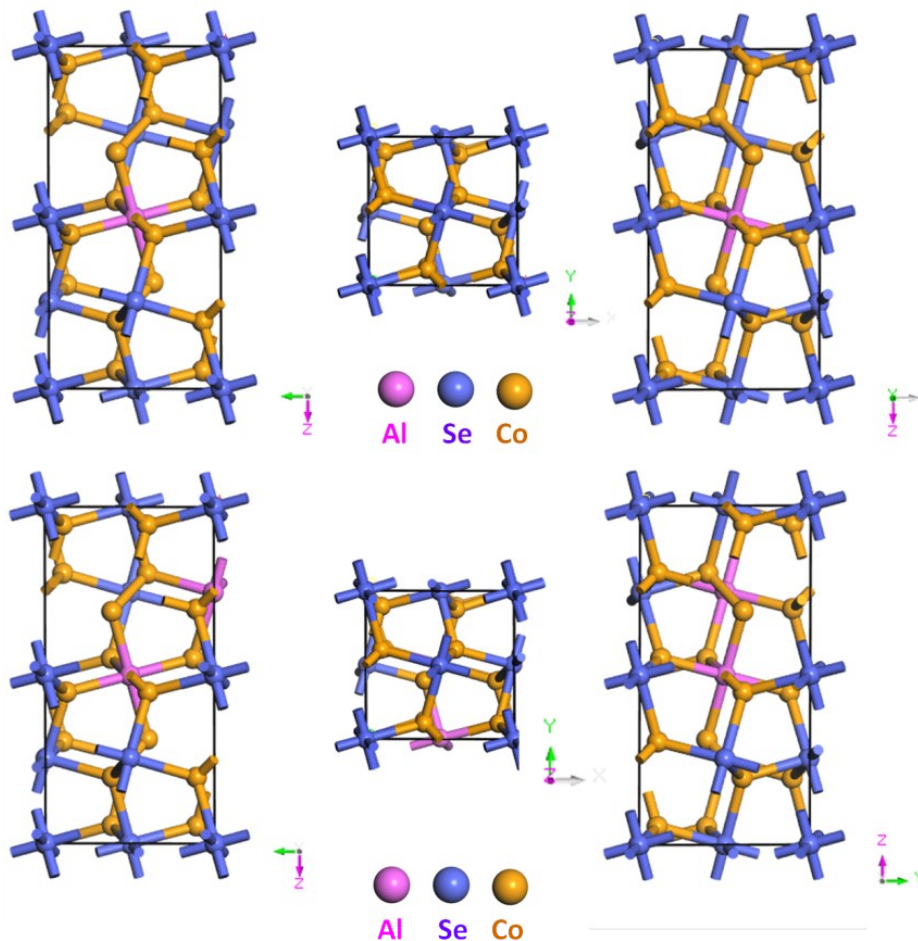
Fig. S9 Illustration of the crystal structures of $AlCo_7Se_{16}$ and $Al_2Co_6Se_{16}$ calculated by DFT-GGA.

Table S1 Calculated lattice parameters, total energy, and volume for Co_8Se_{16}, $AlCo_7 Se_{16}$, and $Al_2Co_6 Se_{16}$

Compound	a (Å)	b (Å)	c (Å)	Total Energy (Ha)	Volume (Å³)
Co_8Se_{16}	5.862	5.871	11.828	-7275.706	406.324
$AlCo_7Se_{16}$	5.827	5.849	11.763	-6673.2493	372.001
$Al_2Co_6Se_{16}$	5.821	5.842	11.775	-6673.2545	371.468

DFT-based first-principle calculations were employed to understand the partial substitution of Co^{2+} by Al^{3+} in $CoSe_2$. Table S1 shows that lattice parameters a, b, and c decreased slightly, whereas the volume and total energy decreased significantly upon replacement of partial Co^{2+} sites with high electric-density and smaller Al^{3+} ions.
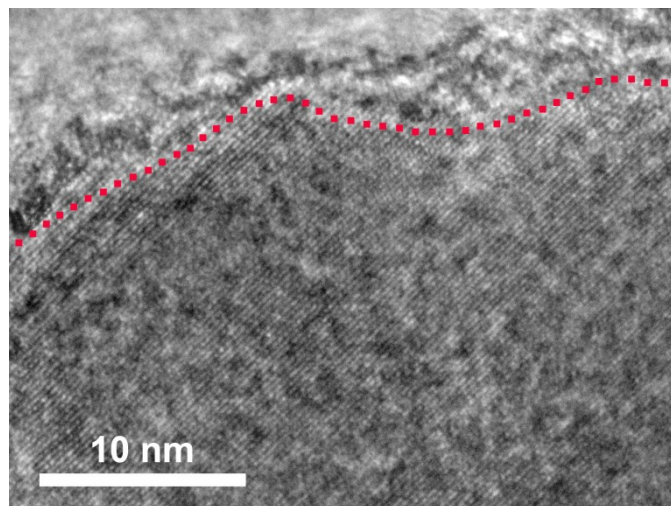
Fig. S10 HRTEM images of fully discharged CoSe$_2$/C-ND electrode after the initial cycle
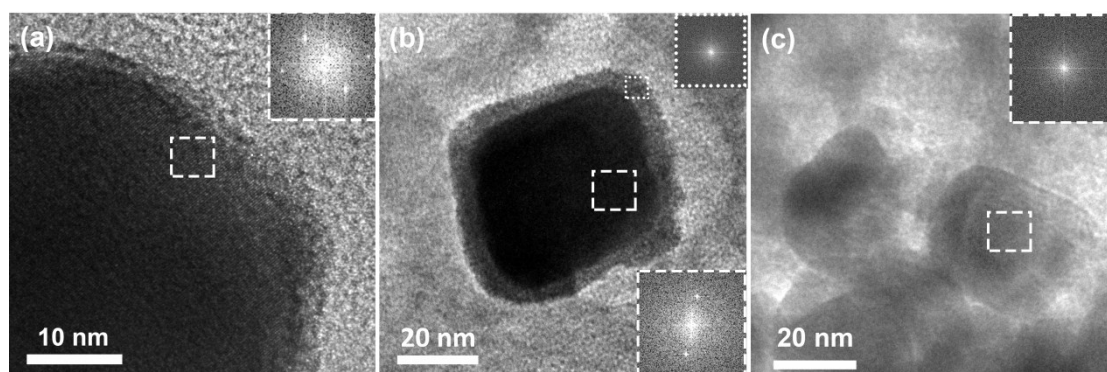
Fig. S11 Low-magnification TEM images of the fully discharged CoSe$_2$/C-ND electrodes after 1 cycle (a), 5 cycles (b), and 100 cycles (c) (Inset: selected-area fast Fourier transforms).

Fig. S12 Photos of ethanol solutions of fresh electrolyte (Ⅰ),electrolyte of a RAIB cell containing a CoSe$_2$/C-ND cathode after fully discharge (Ⅱ), and pure CoCl2 crystalline (Ⅲ)
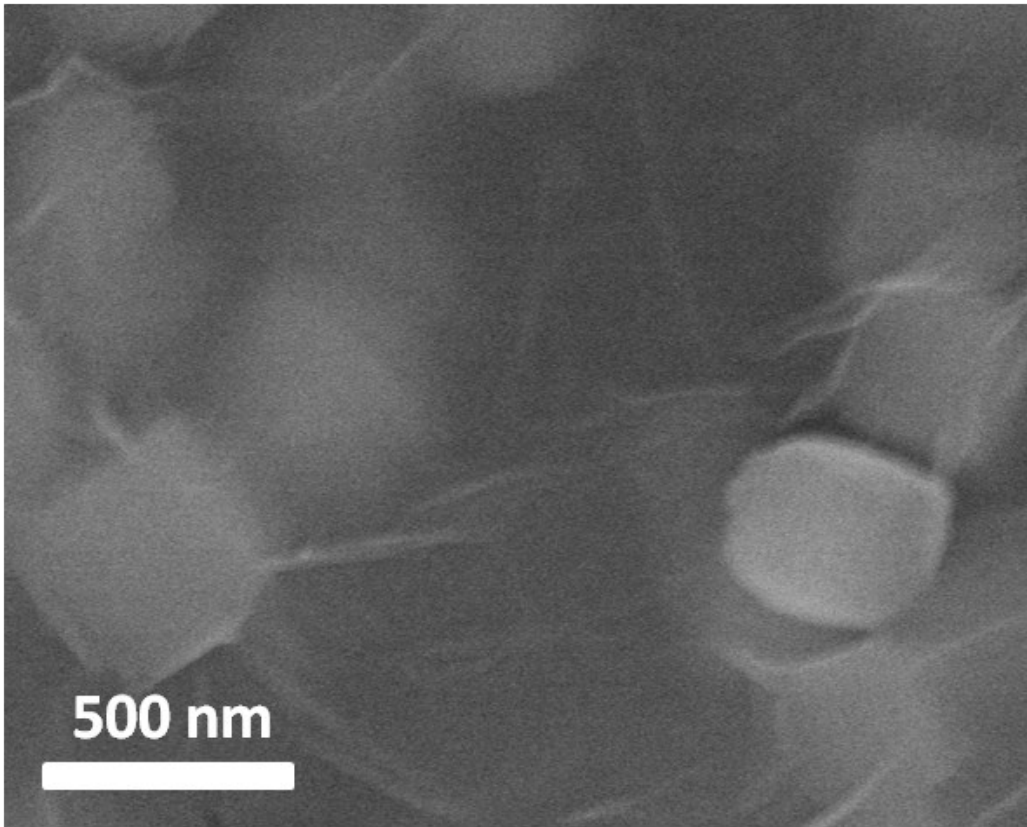
Fig. S13 SEM image of PDDA/CoSe$_2$/C-ND@GO.
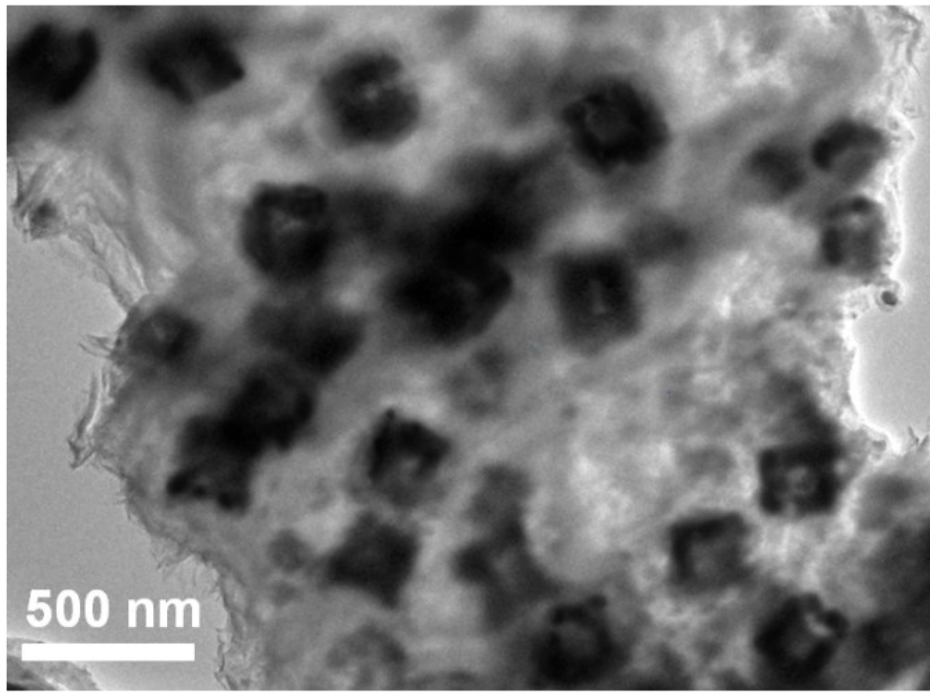
Fig. S14TEM image of CoSe$_2$/C-ND@rGO.
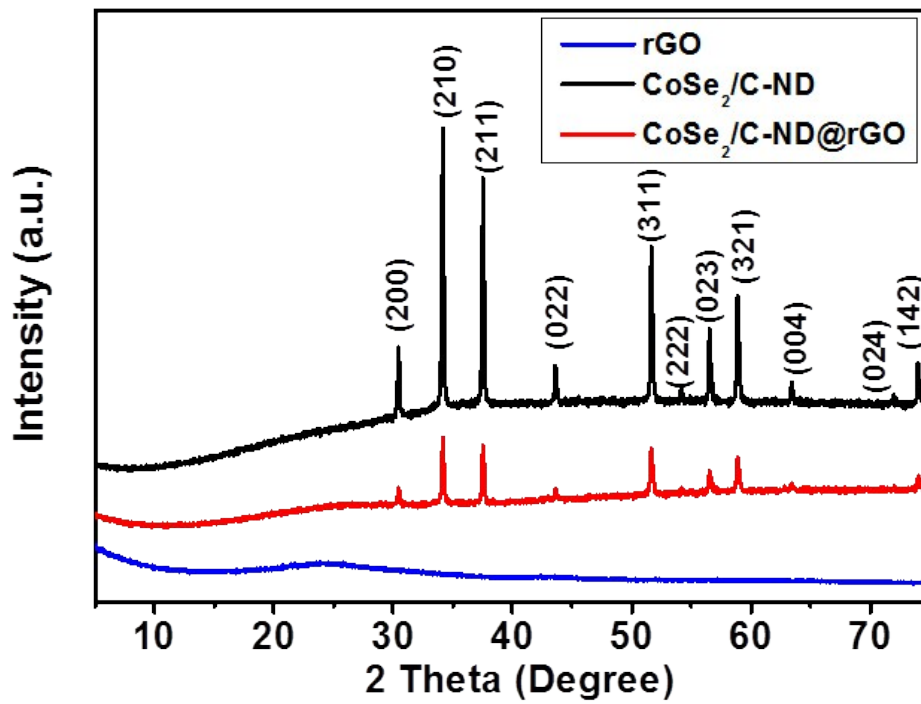
Fig. S15 XRD pattern of pure rGO, CoSe$_2$/C-ND, and CoSe$_2$/C-ND@rGO.
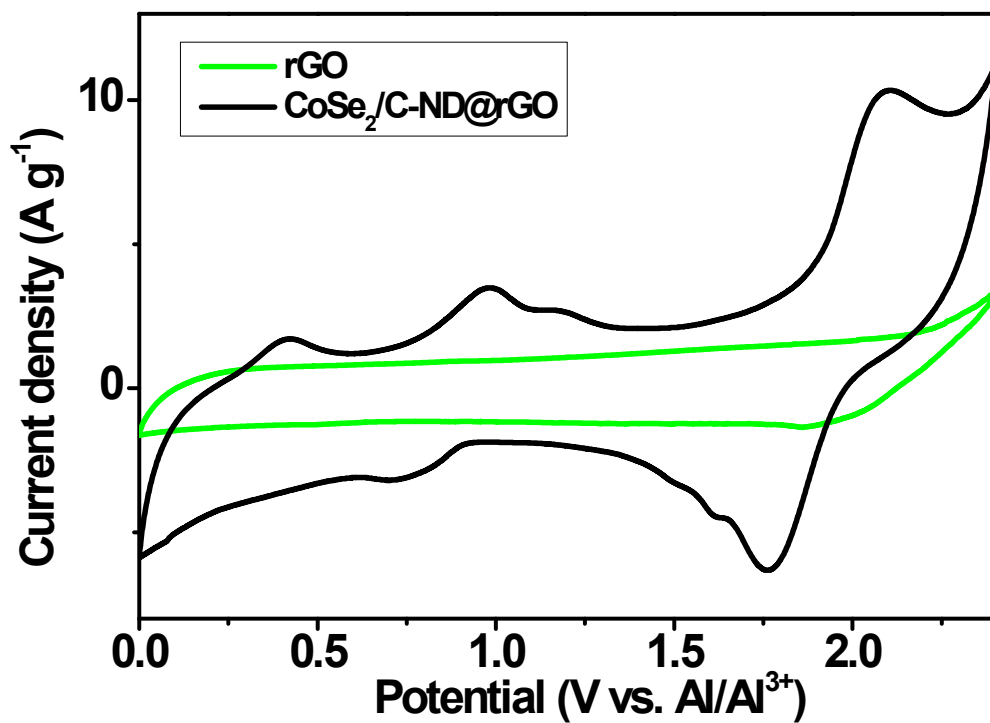
Fig. S16 Typical CV curves of pure rGO and CoSe$_2$/C-ND@rGO cathodes at a scan rate of 10 mV s^{-1}.
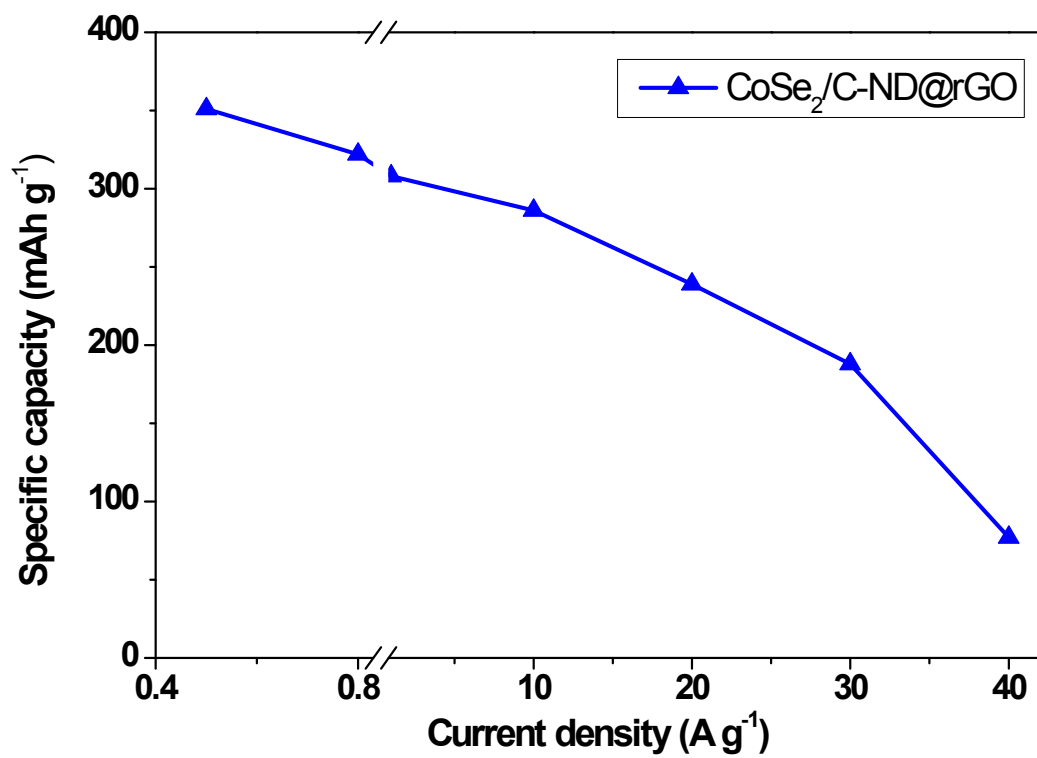
Figure S17 The rate performance of the $CoSe_2$/C-ND@rGO .
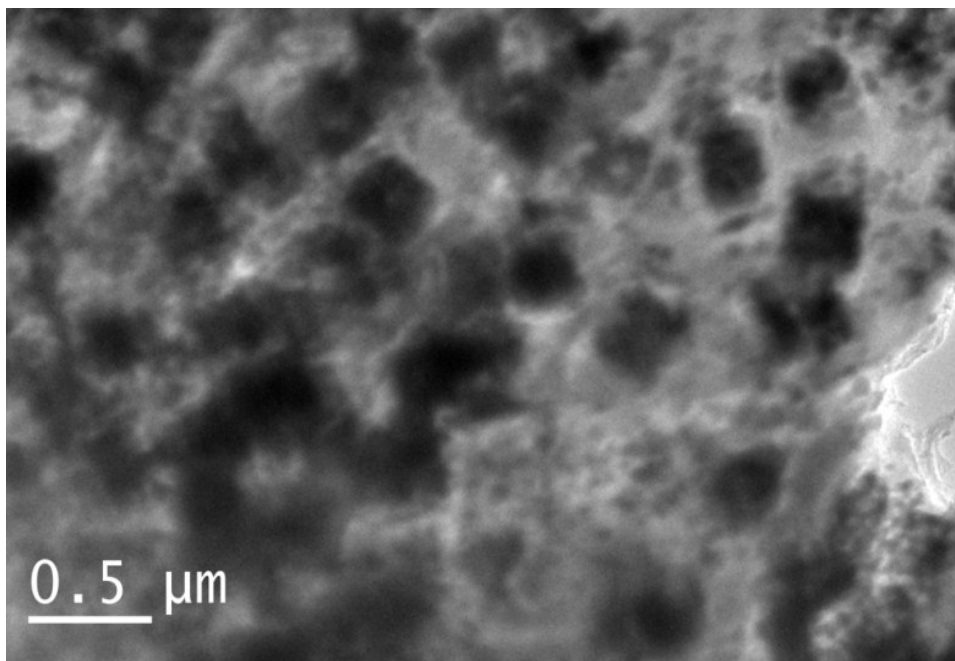
Fig. S18 TEM images of the fully discharged CoSe$_2$/C-ND@rGO electrodes after 500 cycles.
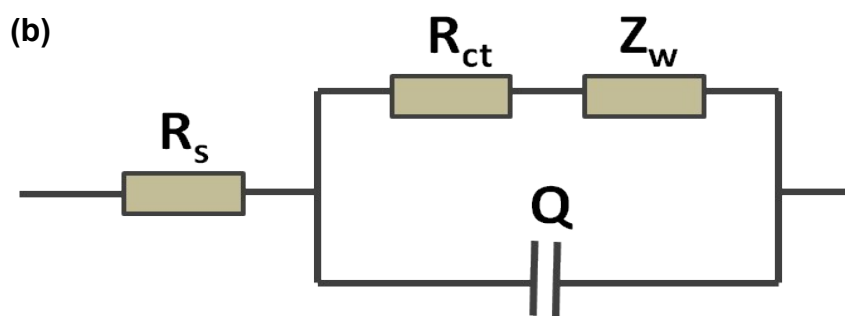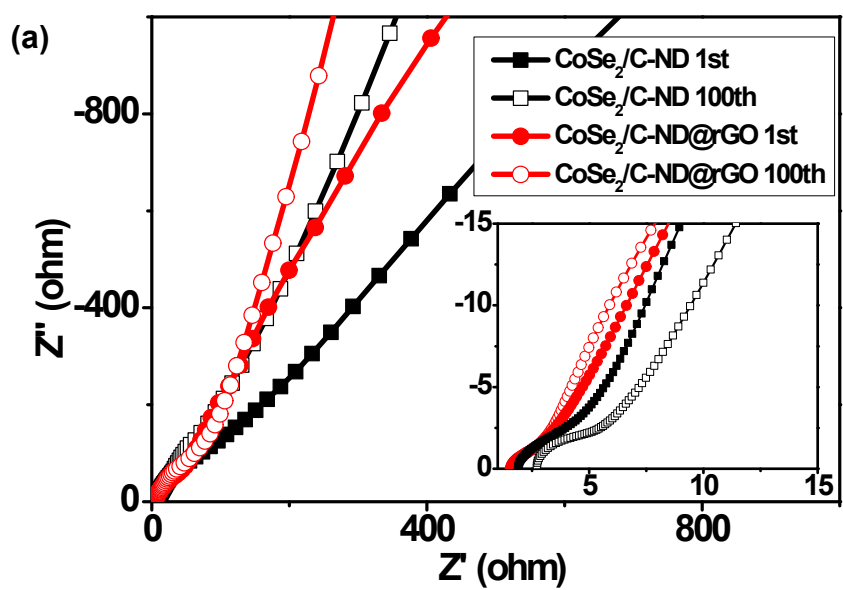
Fig. S19 (a) Nyquist plots of CoSe$_2$/C-ND and CoSe$_2$/C-ND@rGO determined at 1.7 V (inset: enlarged plots) and (b) equivalent circuit model of the studied system.

Table S2 Comparative electrochemical performance of CoSe$_2$/C-ND@rGO with other cathode materials recently reported.

Cathode materials	Electrolyte (molar ratio)	Discharge capacity/mA h g^{-1}		Cycle number	Current density/mA g^{-1}	Discharge voltage (V)	Ref.
		1st cycle	last cycle				
CoSe$_2$/C-ND@rGO	AlCl$_3$: [EMIm]Cl (1.3:1)	326	143	500	1000	1.8	This work
Mo$_6$S$_8$	AlCl$_3$: [EMIm]Cl (1.5:1)	148	70	50	12	0.55	6
Graphitic foam	AlCl$_3$:[EMIm]Cl (1.3:1)	65	65	100	5000	2.0	7
			65	700			
Ni$_3$S$_2$	AlCl$_3$: [EMIm]Cl (1.3:1)	350	60	100	100	1.0	8
CuS@C	AlCl$_3$: [EMIm]Cl (1.3:1)	240	90	100	20	1.0	9
G-SnS$_2$	AlCl$_3$: [EMIm]Cl (1.3:1)	270	70	100	200	0.68	10
Co$_9$S$_8$@CNT–CNF	AlCl$_3$: [EMIm]Cl (1.3:1)	115	87	6000	1000	0.9	11
TiS$_2$	AlCl$_3$: [EMIm]Cl (1.5:1)	70	65	20	5	-	12
V$_2$O$_5$ NW	1.1 : 1 AlCl$_3$: [EMIm]Cl	305	273	20	125	0.5	13
Polypyrrole	AlCl$_3$: [EMIm]Cl (1.5:1)	70	50	100	20	0.8-2.0	14
Polythiophene	AlCl$_3$:[EMIm]Cl (1.5:1)	90	70	100	16	0.8-2.0	14
Carbon paper	AlCl$_3$:[EMIm]Cl (1.3:1)	50	62	50	150	1.8	15
GF-HC	AlCl$_3$:[EMIm]Cl (1.3:1)	120	120	250000	40000	1.8	16
CuHCF	Al(OTF)$_3$:diglyme (50:1)	60	10	10	0.1 C	0.2-0.5	17

Reference

1. H. Hu, J. Zhang, B. Guan and X. W. Lou, *Angewandte Chemie-International Edition*, 2016, **55**, 9514-9518.
2. B. Liu, H. Shioyama, T. Akita and Q. Xu, *Journal of the American Chemical Society*, 2008, **130**, 5390-5391.
3. H. Li, X. Qian, C. Zhu, X. Jiang, L. Shao and L. Hou, *Journal of Materials Chemistry A*, 2017, **5**, 4513-4526.
4. K. Zhang, M. Park, L. Zhou, G.-H. Lee, W. Li, Y.-M. Kang and J. Chen, *Advanced Functional Materials*, 2016, **26**, 6728-6735.
5. J. Li, D. Yan, T. Lu, Y. Yao and L. Pan, *Chemical Engineering Journal*, 2017, **325**, 14-24.
6. L. X. Geng, G. C. Lv, X. B. Xing and J. C. Guo, *Chemistry of Materials*, 2015, **27**, 4926-4929.
7. M.-C. Lin, M. Gong, B. Lu, Y. Wu, D.-Y. Wang, M. Guan, M. Angell, C. Chen, J. Yang, B.-J. Hwang and H. Dai, *Nature*, 2015, **520**, 325-328.
8. Y. Hu, B. Luo, D. Ye, X. Zhu, M. Lyu and L. Wang, *Advanced Materials*, 2017, 1606132-1606137.
9. S. Wang, S. Jiao, J. Wang, H. S. Chen, D. Tian, H. Lei and D. N. Fang, *ACS Nano*, 2017, **11**, 469-477.
10. T. Zhou, W. K. Pang, C. Zhang, J. Yang, Z. Chen, H. K. Liu and Z. Guo, *Acs Nano*, 2014, **8**, 8323-8333.
11. Y. Hu, D. Ye, B. Luo, H. Hu, X. Zhu, S. Wang, L. Li, S. Peng and L. Wang, *Advanced Materials*, 2018, **30**, 103824-103829.
12. L. Geng, J. P. Scheifers, C. Fu, J. Zhang, B. P. T. Fokwa and J. Guo, *Acs Applied Materials & Interfaces*, 2017, **9**, 21251-21257.
13. N. Jayaprakash, S. K. Das and L. A. Archer, *Chemical Communications*, 2011, **47**, 12610-12612.
14. N. S. Hudak, *The Journal of Physical Chemistry C*, 2014, **118**, 5203-5215.
15. H. Sun, W. Wang, Z. Yu, Y. Yuan, S. Wang and S. Jiao, *Chemical Communications*, 2015, **51**, 11892-11895.
16. H. Chen, H. Xu, S. Wang, T. Huang, J. Xi, S. Cai, F. Guo, Z. Xu, W. Gao and C. Gao, *Science Advances*, 2017, **3**.
17. L. D. Reed, S. N. Ortiz, M. Xiong and E. J. Menke, *Chemical Communications*, 2015, **51**, 14397-14400.